Disagreements in Low-Level Moisture between (Re)Analyses over Summertime West Africa

ALEXANDER J. ROBERTS AND JOHN H. MARSHAM

School of Earth and Environment, University of Leeds, Leeds, United Kingdom

PETER KNIPPERTZ

Institute for Meteorology and Climate Research, Karlsruhe Institute of Technology, Karslruhe, Germany

(Manuscript received 26 June 2014, in final form 22 September 2014)

ABSTRACT

Reanalysis and operational analysis products are routinely used as the best estimates of the atmospheric state for operational and research purposes. However, different models, assimilation techniques, and assimilated datasets lead to differences between products. Here, such differences in the distribution of low-level water vapor over summertime West Africa are analyzed, as reflected in the zonal mean position of the leading edge of the West African monsoon [the intertropical discontinuity (ITD)] using five reanalyses [NCEP–NCAR, NCEP–Department of Energy (DOE), the Modern-Era Retrospective Analysis for Research and Applications (MERRA), the Climate Forecast System Reanalysis (CFSR), and the Interim ECMWF Re-Analysis (ERA-Interim)] and two operational analyses [Global Forecast System (GFS) and ECMWF] during the 11 monsoon seasons (April–September) from 2000 to 2010. Specific humidity differences regularly reach 50% of the mean value over areas spanning hundreds of kilometers and often coincide with northward excursions of the ITD that last several days and bring unusual rainfall to the Sahel and Sahara. The largest disagreements occur during the southward retreat of the ITD and are connected with anomalously high values of aerosol optical depth, consistent with the production of haboob dust storms. The results suggest that known errors in the representation of moist convection and cold pools may contribute to the identified disagreements. A large reduction in disagreement occurs in 2006, when upper-air observations were enhanced during the African Monsoon Multidisciplinary Analysis (AMMA) campaign, pointing to an insufficient observational constraint of the (re)analyses in other years. It is hoped that this work will raise awareness of the limited reliability of (re)analysis products over West Africa during the summer, particularly during northward surges of the ITD, and will instigate further work to improve their quality.

1. Introduction

The intertropical discontinuity (ITD) is the interface between the moist southwesterly monsoonal flow and the dry northerly Saharan wind. The ITD can be defined as the confluence of surface winds and also has strong near-surface moisture and temperature gradients. In practice the ITD is more usually recognized as the point at which the near-surface dewpoint temperature is equal to 14°C. Over the boreal summer the ITD moves north over West Africa, bringing moist air from the Gulf of Guinea and the Atlantic Ocean far inland. The monsoon then retreats during and after September (Sultan and Janicot 2000). The position of the ITD also has a strong diurnal dependence (Parker et al. 2005; Sultan et al. 2007; Pospichal et al. 2010). Dry convective turbulence produced by surface heating raises the turbulent viscosity of the monsoon flow, suppressing circulation during the day. At night the increased stability allows for the monsoon front to advance north under the influence of the Saharan heat low (SHL) (Parker et al. 2005; Burton et al. 2013).

The ITD is dynamic, influenced by synoptic- and mesoscale meteorology. Processes that are known to influence the position of the ITD include interactions with the extratropics (Knippertz 2008; Vizy and Cook 2009; Knippertz and Todd 2010; Roehrig et al. 2011;

Roberts and Knippertz 2014), changes to the strength of the SHL (Parker et al. 2005), African easterly waves (AEWs) on the African easterly jet (AEJ) (Berry and Thorncroft 2005; Couvreux et al. 2010; Bain et al. 2011), convectively generated cold pools (Flamant et al. 2007; Cuesta et al. 2010; Marsham et al. 2008, 2013b; Garcia-Carreras et al. 2013; Roberts and Knippertz 2014), and eastward-propagating convectively coupled Kelvin waves (Mounier et al. 2007; Mekonnen et al. 2008; Mera et al. 2014). Increased boundary layer moisture south of the ITD, in regions where the monsoon flow is deep, allows for the production of mesoscale convective systems (MCSs). Therefore, the spatial and temporal distribution of precipitation is strongly influenced by the behavior of the ITD. It has been shown by Mohr et al. (1999) that African MCSs are responsible for approximately 80% of annual rainfall between 5° and 18°N. This makes the ITD especially important in the Sahel, whose inhabitants are heavily dependent on rain-fed agriculture. Additionally, the collapse of seasonal outbreaks of meningitis that affect the Sahel have been shown to be strongly linked to increases in humidity associated with northward surges of the monsoon flow (Mera et al. 2014; Pandya et al. 2015). These impacts on West African meteorology mean that there is great value in understanding the behavior of the ITD in models, observations, and such widely used products as operational analysis and reanalysis datasets.

The ITD is also an important feature in mineral dust uplift. MCSs in the northern Sahel and southern Sahara are capable of lifting large amounts of dust through the production of convective cold pools known as haboobs (Sutton 1925; Hamilton et al. 1945; Flamant et al. 2007; Marsham et al. 2008; Roberts and Knippertz 2012; Marsham et al. 2013b). The monsoon front has also been implicated in dust-lifting processes (Bou Karam et al. 2008; Marsham et al. 2008; Burton et al. 2013). Airborne mineral dust is a major source of uncertainty in our understanding of the climate system (Solomon et al. 2007). Poorly defined dynamics of dust uplift, impacts of direct and indirect radiative properties, and the role of dust in the biogeochemical cycle means that study of the meteorological processes in the world's largest source of mineral dust is important (Knippertz and Todd 2012).

Global reanalysis and operational analysis products [collectively referred to as (re)analysis products hereafter] aim to provide the best estimate of the state of the atmosphere using both a short forecast and available observations. They are used to initialize operational numerical weather prediction simulations, drive chemistry transport models (e.g., Chipperfield 2006; Emmons et al. 2010; Huijnen et al. 2010), and initialize high-resolution limited-area simulations for research (e.g., Knippertz et al. 2009; Reinfried et al. 2009; Solomos et al. 2012; Roberts and Knippertz 2014). Marsham et al. (2011) highlight disagreement between analyses in the Saharan heat low region. Birch et al. (2013), Schepanski et al. (2014), and Roberts and Knippertz (2014) highlight the sensitivity of high-resolution simulations over West Africa to differing initial conditions from (re)analysis products. In Roberts and Knippertz (2014) several products [the Global Forecast System operational analysis, the Interim European Centre for Medium-Range Weather Forecasts (ECMWF) Re-Analysis (ERA-Interim), and the ECMWF operational analysis] were used to initialize high-resolution simulations using the same Weather Research and Forecasting Model setup. In only one of these simulations did the MCS being investigated develop similarly to the observed system. The differences between simulations initialized with different products were larger than those from changing the model physics, suggesting that there are significant inconsistencies between the products commonly used for model initialization.

The (re)analysis products are generated by running a short forecast from the previous analysis time and assimilating observations to correct the model's first guess. Over large parts of West Africa there are very few in situ observations, especially in the Sahel and Sahara (Fig. 1). Therefore, (re)analysis products are poorly constrained and the paucity of the observational network in parts of West Africa means that the evaluation of products is not trivial. In the Sahara, ground and upper-air observations are particularly sparse as a result of both the inhospitable environment and the politics of the region, making (re)analyses heavily reliant on satellite data. Those satellites, however, have difficulties in retrieving near-surface water vapor (Urban 2013). An example of the influence of upper-air observations on a coarse-resolution model in a data-poor region can be seen in Garcia-Carreras et al. (2013). Simulations using the operational Met Office Unified Model at 30-km grid spacing show that the 925-hPa potential temperature around Bordj Badji Mokhtar in Algeria (21.4°N, 0.9°E) is strongly influenced by the assimilation of radiosonde soundings to an approximate diameter of 500 km. The impact of a greater number of observations in this region is also shown in Agustí Panareda et al. (2010a,b), who show significant improvements to the ECMWF reanalysis. These improvements are achieved through the assimilation of additional observations, which were made as part of the African Monsoon Multidisciplinary Analysis (AMMA) field campaign during the summer of 2006.

Recent studies have shown the direct impact of organized convection on the West African monsoon (WAM) and the location of the ITD, and that global models struggle to capture these impacts. Flamant et al.
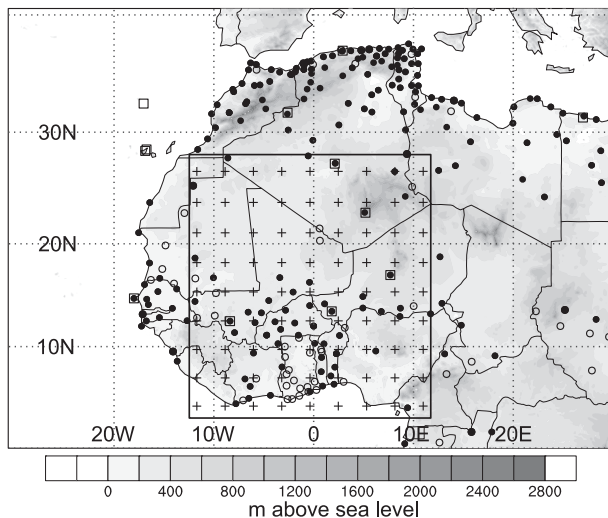
FIG. 1. Geographical overview of West Africa. Terrain height is indicated by shading, also shown is the box bounding the area being studied (3°–28°N and 12°W–12°E) with crosses to show the points onto which (re)analysis data have been regridded. Squares represent radiosonde stations that launched an average equal to or exceeding one sonde per day (based on the Integrated Global Radiosonde Archive) April–September 2000–10. The circles represent surface synoptic observation (SYNOP) stations: unfilled circles reported on at least 25% of the (re)analysis times, and filled circles on at least 50% of the (re)analysis times being studied (based on data from the Met Office Integrated Data Archive System).

(2007) showed how a cold pool outflow from an MCS formed the leading edge of the monsoon (ITD) for one case during the AMMA field campaign. Comparing simulations with parameterized and explicit convection and observations, Marsham et al. (2013a) show that the representation of convection has impacts on the entire WAM and its diurnal cycle, and that cold pools contribute a substantial part of the monsoon flow in explicit simulations, but are missing when convection is parameterized. This is consistent with recent observations from the central Sahara showing that cold pools contribute significantly to meridional water vapor transport and that their absence appears to be a major cause of global model bias (Marsham et al. 2013a; Garcia-Carreras et al. 2013). This absence of cold pools leads to major biases in dust, as haboobs are essentially missing (Marsham et al. 2011; Heinold et al. 2013).

It is assumed in this study that particular meteorological conditions make it particularly hard to produce a consistent ensemble of (re)analyses leading to situations of large disagreement. The investigation of periods of disagreement, and the weather associated with them, provides clues as to the process errors leading to model deviation, as well as motivation for future work into improving their representation in models.

In this study the position of the ITD is estimated in seven (re)analysis products (see section 2) during 11 monsoon seasons (April–September 2000–10). We aim to answer the following questions: 1) How big are the differences between products? 2) Where and when are the disagreements in ITD positions greatest? 3) Under what meteorological conditions do episodes of high disagreement occur? It is important to note that agreement between products does not imply that they are correct. Disagreement, on the other hand, points to differences in model first guesses or in the ability to assimilate the available data.

2. Data and methods

The (re)analysis products used in this study are 1) the National Centers for Environmental Prediction (NCEP)–National Center for Atmospheric Research (NCAR) 40-Year Reanalysis (NCEP–NCAR hereafter; Kalnay et al. 1996; Kistler et al. 2001), 2) the NCEP–Department of Energy (DOE) Reanalysis 2 (NCEP–DOE hereafter; Kanamitsu et al. 2002), 3) the NCEP Climate Forecast System Reanalysis (CFSR; Saha et al. 2010), 4) the National Aeronautics and Space Administration's (NASA) Modern-Era Retrospective Analysis for Research and Applications (MERRA; Rienecker et al. 2008, Rienecker et al. 2011), 5) the ECMWF ERA-Interim (ERA-Int hereafter; Dee et al. 2011), 6) the ECMWF operational analysis (ECMWF-op hereafter), and 7) the NCEP Final (FNL) operational Global Forecast System (GFS) analysis. Details of all these products can be found in Table 1.

As the ECMWF-op and GFS products are operational analyses, the models used to create them have been developed over time, changing considerably during the 11-yr period being investigated. Further information on the development of ECMWF-op and GFS can be found online (http://www.ecmwf.int/products/data/technical/model_id/index.html and http://www.emc.ncep.noaa.gov/gmb/STATS/html/model_changes.html, respectively).

For observations of precipitation, Tropical Rainfall Measuring Mission (TRMM) 3B42 V7 rainfall retrievals are used. This product uses a combination of spaceborne radar, and microwave and infrared radiance data, to create 3-hourly rainfall estimates at 0.25° × 0.25° resolution (Huffman et al. 2007). A limitation of TRMM is that over the period being studied the availability of satellite products has varied (primarily due to the introduction of new satellites), meaning that accuracy varies with time. Despite this, the spatial and temporal coverage of infrared measurements from geostationary satellites, and a strong correlation between rainfall and cloud-top temperatures, mean that TRMM is considered sufficient to detect the presence of deep clouds capable of generating convective rainfall. Another limitation of TRMM is that when high

TABLE 1. Details of the seven (re)analysis products including the name used in the text, the center that produced the (re)analysis, the (re)analysis type, start and end years, and the horizontal and vertical resolutions.

Name	Center	Type	Start	End	Horizontal	Vertical
NCEP–NCAR	NCEP	Reanalysis	1948	Present	T62 ~200 km	28 levels
NCEP–DOE	NCEP	Reanalysis	1979	2012	T62 ~200 km	28 levels
CFSR	NCEP	Reanalysis	1979	2010	T382 ~30 km	64 levels
MERRA	NASA	Reanalysis	1979	Present	1/2° lat ~55 km 2/3° lon ~75 km	72 levels
ERA-Int	ECMWF	Reanalysis	1979	Present	T255 ~80 km	60 levels
ECMWF-op	ECMWF	Operational analysis	—	—	Variable	Variable
GFS	NCEP	Operational analysis	—	—	Variable	Variable

quality rainfall data are unavailable (when the product relies on radiances from geostationary satellites), there is no information about the distribution of hydrometeors throughout the vertical column. In the Sahara and Sahel, where deep dry boundary layers are common, there is likely to be a high rate of precipitation evaporation. This means that the quantity of precipitation that reaches the surface might be very different from that estimated by the TRMM 3B42 V7 product. However, with respect to this study discrepancies caused by evaporation are not important as TRMM is used to indicate the presence of convective systems and not to determine the amount of rainfall reaching the surface.

The box marked in Fig. 1 shows the region being studied (3°–28°N, 12°W–12°E). This box covers the latitudinal range of the monsoon flow, including the Gulf of Guinea coast, the Soudan zone, the Sahel, and the southern to central Sahara. All products are regridded to approximately 2.5° × 2.5° to match the coarsest-resolution products (NCEP–NCAR and NCEP–DOE), producing the 9 × 9 grid shown in Fig. 1. For each (re)analysis product and time, the edge of the monsoon flow is estimated by zonally averaging the 925-hPa specific humidity (q_{925}) and finding the latitudinal position where it reaches $10\,\mathrm{g\,kg^{-1}}$ by linear interpolation. As mentioned above, the ITD is more usually defined by the confluence of low-level winds, a strong gradient in moisture or temperature, or a surface dewpoint temperature of 14°C. The $10\,\mathrm{g\,kg^{-1}}$ method used here for the identification of the edge of the monsoon flow on a large scale gives similar results to the ITD position found from the maximum latitudinal gradient of q_{925} and the total-column water vapor. However, the confluence of near-surface winds compares less favorably. This lack of agreement is not seen as a problem in this study as we are focused on the distribution of low-level water vapor since this has a strong influence on convective initiation and development (arguably the most important meteorological features in this region). Despite the use of a threshold value (which is typically a little drier than a surface dewpoint of 14°C), this metric is a useful indicator of the large-scale latitude to which moisture advection by the monsoon flow

is important. Therefore, the single latitude value generated for each product at each time gives a measure of the approximate ITD position across the zonal range of the box and will be referred to as ITDΦ hereafter. To check whether differences between ITDΦs in different (re)analysis products are controlled by the position of their ITD or by large-scale moisture biases, the root-mean-square difference (RMSD) of q_{925} is calculated. Thereby, each product is compared to the mean q_{925} field calculated from all seven products, indicating the difference between a product and the ensemble mean. Figure 2 shows the RMSD for each product averaged over all the times in the study. There is a clear pattern in the distribution of high values, with the majority occurring between 10° and 20°N. This coincides with the climatological position of the ITD over the monsoon season (Sultan and Janicot 2000). CFSR has the highest RMSD values, suggesting that its q_{925} deviates from the ensemble mean by a larger amount and/or more frequently than do the other products in this region. The low RMSD values to the north and south, present in most products, show that these regions are far less likely to have interproduct disagreements in low-level moisture. The high RMSD values over the Gulf of Guinea in NCEP–NCAR show that this product has a moisture bias not associated with the monsoon front. This is in agreement with Trenberth and Guillemot (1995), who identified large and significant moisture biases in NCEP–NCAR over the tropics.

3. Characteristics of the disagreement between (re)analysis products

To identify likely periods of ITD disagreement, the standard deviation σ of ITDΦ values across (re)analyses is calculated using the ITDΦs at each 6-hourly (re)analysis time. The top 5% of σ values across all 11 monsoon seasons are then used to detect the periods of strongest disagreement. By identifying when these events occur and by investigating the meteorology at these times, the specific conditions that produce disagreement can
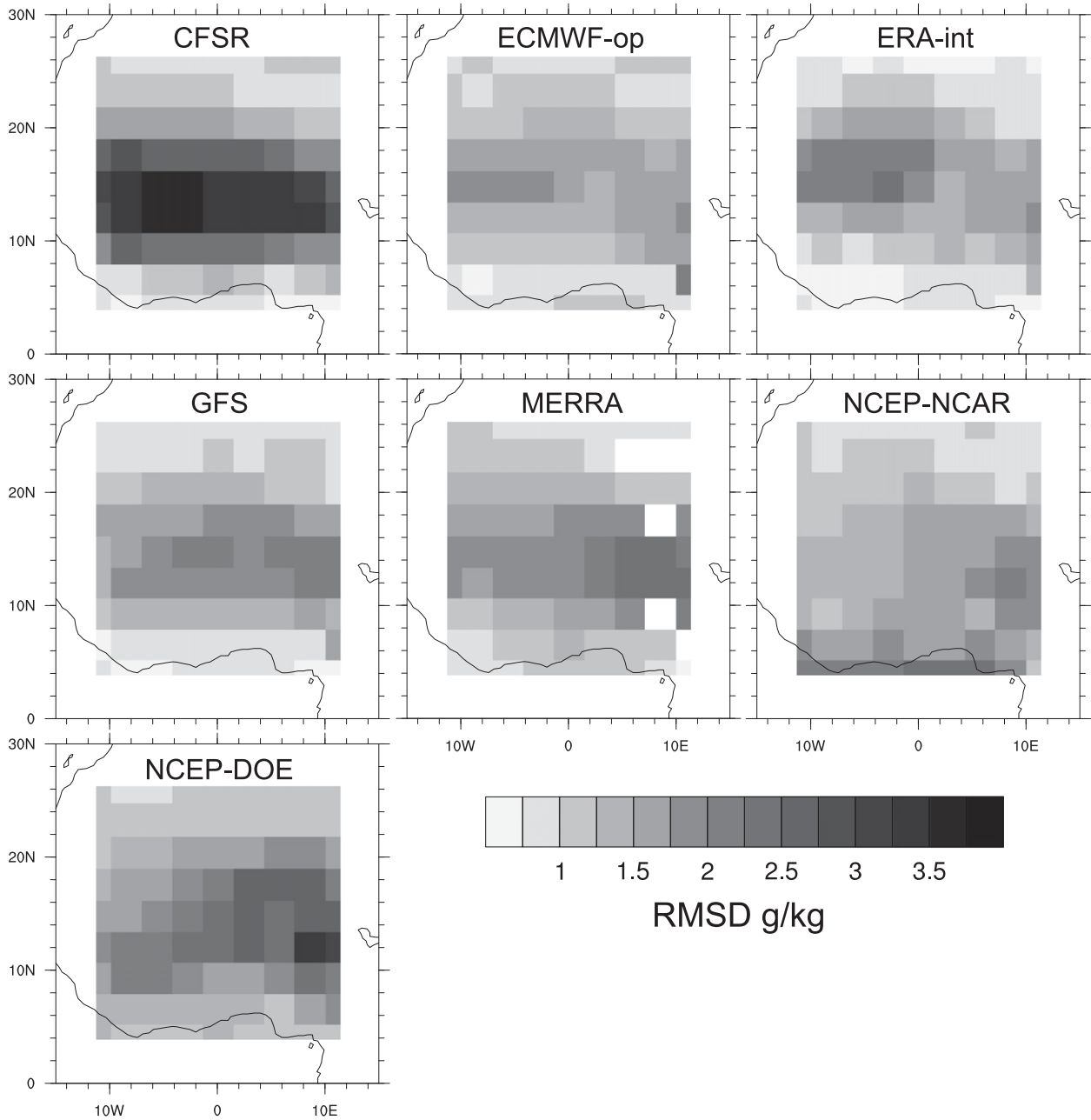
FIG. 2. RMSD of 925-hPa specific humidity (q_{925}) relative to the mean q_{925} of all products averaged over the monsoon season April–September 2000–10. For abbreviation of product names see section 2.

be identified. Figure 3 shows an example time series of ITDΦ in each product (colored lines) and σ (black dashed line) for the 2010 monsoon season. The gray areas indicate periods where the disagreement between products produces σ values in the top 5% of σ values across all 11 yr. Figure 3 also shows the northward progression and then the southward retreat of the ITDΦ through the season. It can be seen that large disagreements tend to

occur during northward shifts in the ITDΦ, which last between 1 and 8 days. More systematic analysis of this trend is made in subsequent sections.

a. Magnitude and distribution

As an example, Fig. 4 shows difference plots between three (re)analyses at 0000 UTC 7 June 2010, the initialization time used for the high-resolution limited-area
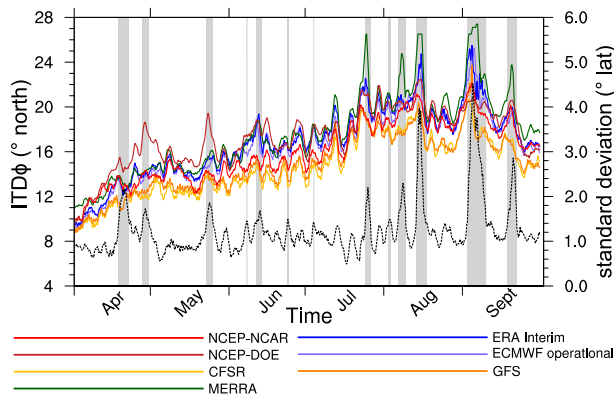
FIG. 3. Behavior of the zonal mean ITDΦ for 2010. Shown is the ITDΦ for all seven reanalysis products (colored lines), the standard deviation calculated from ITDΦs (excluding CFSR, dashed black line), and periods when the standard deviation exceeds the threshold and is in the top 5% of standard deviation values across all 11 yr (gray shading).

simulation of Roberts and Knippertz (2014). To aid interpretation, an image from the Meteosat Second Generation (MSG) Spinning Enhanced Visual and Infrared Imager (SEVIRI) channel 7 (8.30–9.10-μm thermal infrared) is shown for the same time (Fig. 4a). There is a region of convective clouds toward the western coast that is associated with a northward bulge of the monsoon flow in all the products shown in Fig. 4. This northward bulge is produced by low-level winds associated with an anomalous wave on the subtropical jet, which was also linked to the production of precipitating clouds over the Sahel [a tropical plume; Knippertz and Martin (2005)]; these events are discussed in detail in Roberts and Knippertz (2014). Shown in Figs. 4b–d are the differences in q_{925} between ECMWF-op and ERA-Int, MERRA and ERA-Int, and MERRA and CFSR (all regridded onto a 2.5° × 2.5° grid). The estimated position of the ITD in each product is also displayed (based on a q_{925} 10 g kg^{-1} isopleth). Gray areas indicate where the 925-hPa level in either product is below the ground surface and stippled areas show where the difference between the products is greater than 50% of the mean value of the two products.

The deformation of the monsoon flow away from its climatological, zonal configuration can be seen in all four products by the 10 g kg^{-1} isopleths (Figs. 4b–d). Figure 4b shows the difference between ECMWF-op and ERA-Int. Both are produced by ECMWF and have similar model physics and data assimilation methods. There are relatively small differences between these products. In q_{925}, the differences are largest close to the edge of the monsoon flow. In particular, ERA-Int has over 3 g kg^{-1} higher q_{925} compared to ECMWF-op across Niger. Figures 4c and 4d show the difference

between MERRA and ERA-Int and MERRA and CFSR, respectively. The comparison between MERRA and ERA-Int (Fig. 4c) shows a greater range of q_{925} differences compared to Fig. 4b. ERA-Int has values over 3 g kg^{-1} higher than ERA-Int in the northward perturbation of the monsoon flow. Similarly to Fig. 4b, the positions of the two 10 g kg^{-1} isopleths in Fig. 4c are quite close together. However, over Mauritania, eastern Niger, and Chad the ITD in MERRA is farther north than in ERA-Int by as much as 300 km.

The comparison between MERRA and CFSR shows very large differences in q_{925} (Fig. 4d). The differences associated with the northward perturbation of the monsoon flow are large; MERRA has values over 6 g kg^{-1} higher than CFSR in this region. There are also large differences in the region between the two ITD positions over much of the longitudinal extent of West Africa. MERRA positions the ITD approximately 200–300 km farther north than CFSR, producing q_{925} differences of over 8 g kg^{-1}, with differences of over 6 g kg^{-1} covering very large areas of southern Niger and northern Chad. The magnitude of these differences represents a large fraction of the typical values for the Sahel (between 5 and 25 g kg^{-1}), as shown by the widespread stippled regions in Fig. 4d. It should be noted that there are differences in q_{925} over the Atlantic close to the Moroccan coast. These are present in Figs. 4c and 4d, but do not appear to be linked to the behavior of the monsoon flow. Instead, the flow in this region is more likely to be controlled by midlatitude weather systems and the Azores high.

b. Biases

Figures 5a–g show the ITDΦ for each product plotted against the mean ITDΦ calculated from all other products. Every point in each panel represents a single (re)analysis time (0000, 0600, 1200, or 1800 UTC) for each of the 183 days that makes up the monsoon season (April–September) for the 11 monsoon seasons. Shown in each plot is a diagonal line that represents perfect agreement between each product and the mean of the other products, the percentage of points above the diagonal, a Pearson correlation coefficient r, and the slope of the least squares linear trend. All products display high r values (over 0.93), showing that there is very good agreement with respect to the dominating seasonal behavior of the ITDΦ. ECMWF-op and ERA-Int both score particularly highly (0.97) and are closest to the diagonals. The slopes too are all close to 1, suggesting that the direction and magnitude of the dominating seasonal movement is similar in all products. CFSR and GFS produce the lowest slope values, 0.83 and 0.87, respectively. This, and the position of their points with respect to the diagonal show that their
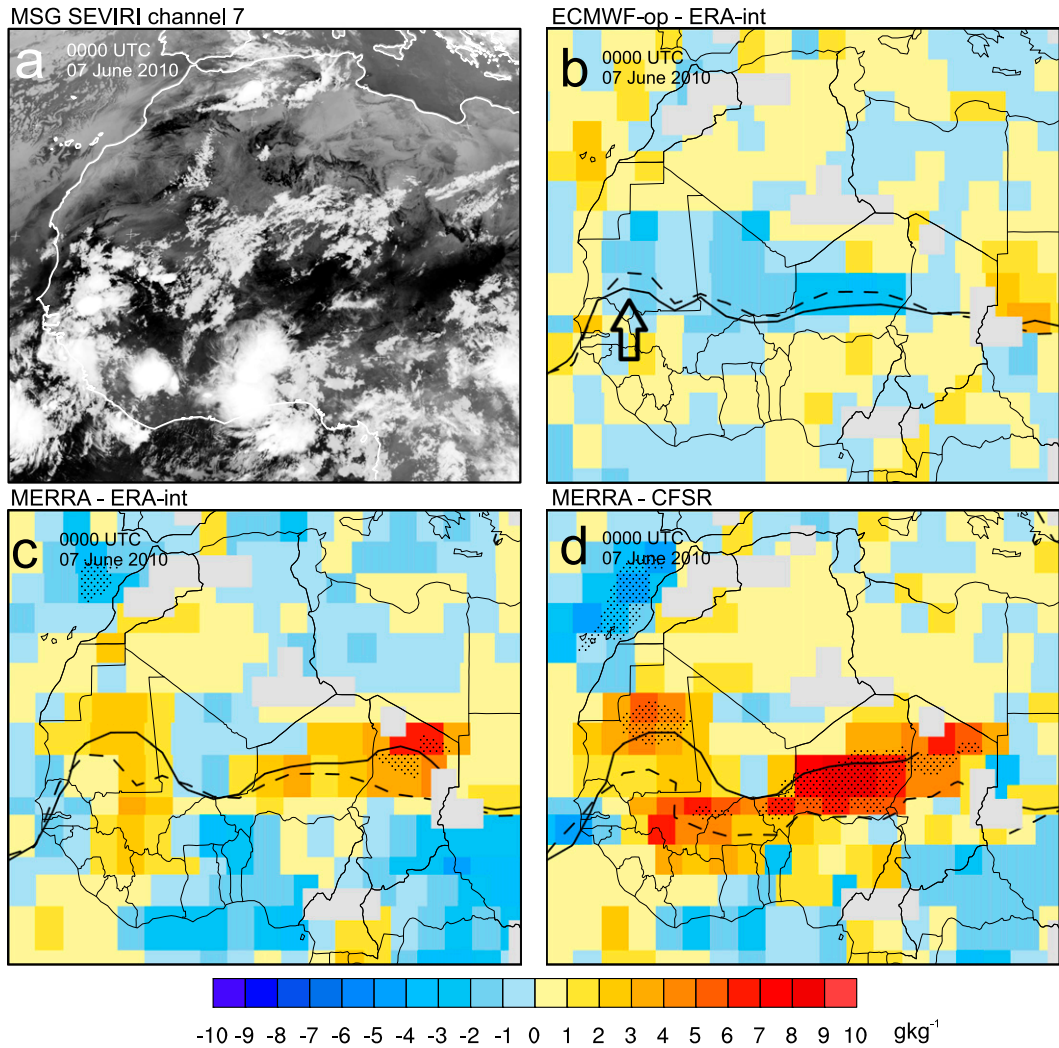
FIG. 4. Magnitude and distribution of disagreement of low-level moisture at 0000 UTC 7 Jun 2010. (a) Meteosat Second Generation (MSG) SEVIRI channel 7 (8.3–9.10-μm thermal IR) image. Difference plots of 925-hPa specific humidity (q_{925}) for (b) ECMWF-op and ERA-Int, (c) MERRA and ERA-Int, and (d) MERRA and CFSR. Black lines represent the q_{925} 10 g kg^{-1} isopleth in both products shown in each panel (solid line for the first product in the plot label, dashed for the second). Gray areas indicate where the 925-hPa pressure surface in either of the products intersects with the ground, while stippled regions indicate where the difference between products is greater than 50% of the mean value.

ITDΦs are likely to be farther south compared to those in other products when the monsoon flow reaches especially far north. CFSR has all but 0.14% of the points below the diagonal, showing that its ITDΦ is systematically farther south compared to the mean of the other products (between 100 and 200 km). This feature can also be seen in Fig. 6a, which shows the mean difference between each product's ITDΦ and the mean of all the other products for all 11 monsoon seasons. In Fig. 6a the CFSR ITDΦ is clearly positioned much farther south than most of the other products in all years; however, it shows a slight reduction in this difference over time (possibly driven

by the introduction of new satellite data). This offset of the ITDΦ represents a low-level moisture bias over West Africa in the CFSR compared to other products. Similarly, both Janiga and Thorncroft (2013) and Lorenz and Kunstmann (2012) have shown a rainfall bias in CFSR over West Africa compared to both observations and other reanalysis products. It is highly likely that the differential representation of the monsoon between products has a strong influence on their respective rainfall distributions. Another striking feature in Fig. 6a is the variation in GFS behavior, showing a southward-displaced ITDΦ in 2000 and 2007–10. Given that it is an
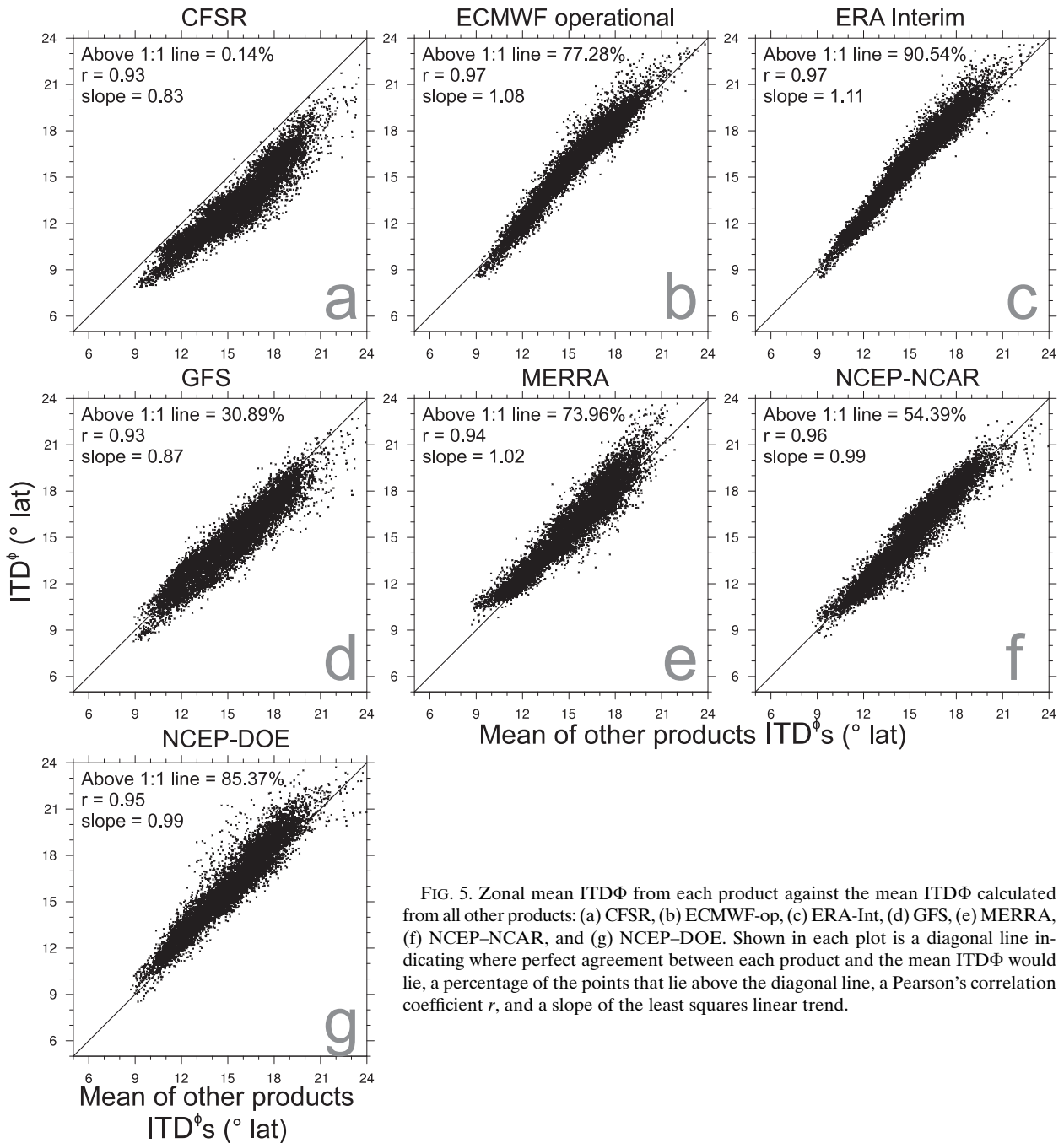
FIG. 5. Zonal mean ITDΦ from each product against the mean ITDΦ calculated from all other products: (a) CFSR, (b) ECMWF-op, (c) ERA-Int, (d) GFS, (e) MERRA, (f) NCEP–NCAR, and (g) NCEP–DOE. Shown in each plot is a diagonal line indicating where perfect agreement between each product and the mean ITDΦ would lie, a percentage of the points that lie above the diagonal line, a Pearson's correlation coefficient r, and a slope of the least squares linear trend.

operational product, possible reasons for this include changes to the GFS model or data assimilation technique, changing satellite data, or different meteorological conditions from year to year. In Fig. 5d we can see that 31% of the GFS points are above the diagonal. This is relatively low when we consider the influence that CFSR has on the mean ITDΦ. Figure 5g shows that NCEP–DOE's ITDΦ is sometimes much farther north than the other products. While the magnitude of this

difference can be hundreds of kilometers, the occurrence of such behavior is rare.

c. Interannual variations

To ascertain whether certain years produce higher or lower levels of disagreement, two measures are used. Figure 6b shows the mean σ (black line) and the proportion of times σ is in the top 5% (gray line; see section 3) for each of the 11 monsoon seasons being studied. Both
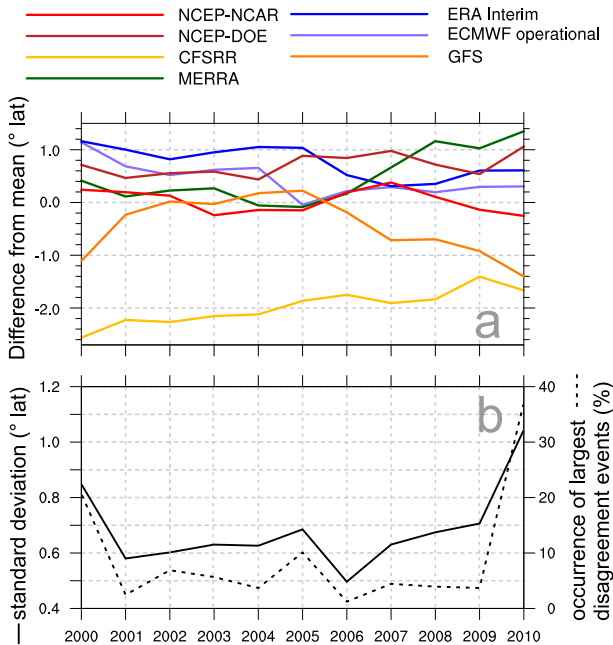
FIG. 6. Interannual behavior of zonal mean ITDΦ. (a) The mean displacement of the zonal mean ITDΦ from the mean ITDΦ of the other products. (b) The standard deviation σ averaged over the monsoon season (solid line) and the percentage of times that it exceeded the extreme disagreement threshold for each year (dashed line; see section 3 for details). Both measures in (b) have been calculated without CFSR because of the systematic bias it displays.

measures have been calculated without using CFSR due to the systematic bias discussed in section 3. Figure 6b shows that the lowest scoring year in both metrics is 2006. Its mean σ across the entire monsoon season is approximately 0.5° latitude and contains less than 2% of the highest-ranking disagreement events. This is much smaller than $^1/_{11}$ of the events (9.1%), which would be expected if the extreme events were distributed evenly. Other years that stand out are 2000 and 2010 with increased disagreement in both metrics. By comparison of 6-hourly time series of different ITDΦs and σ, such as those shown in Fig. 3 for 2010, it appears that the high σ values in 2000 are primarily the result of the GFS ITDΦ being south of the other products, with its behavior closely resembling that of the CFSR for extended periods. This raises the mean σ value over the season to approximately 0.85° latitude compared to the values seen in most other years (between 0.6° and 0.7° latitude). It also means that when other products display disagreement with one another in the year 2000, σ is more likely to be within the top 5% of values across all 11 yr. Over 20% of the highest-ranking disagreement times occur in 2000.

From 2007 to 2010 GFS behaves similarly to how it did in 2000, being farther south than other products (see

Fig. 6a). However, it is only in 2010 that σ and the proportion of top disagreement times is significantly increased. The high values for these measures in 2010 appear to be driven by a number of discrete events. These are responsible for large differences between the products' ITDΦ and, therefore, produce spikes in σ over several days (see Fig. 3). The impact this has is to raise the mean monsoon season σ to over 1° latitude and the percentage of top disagreement times occurring in 2010 to over 35%. The events that produce these large spikes in disagreement in 2010 and other years are predominantly associated with northward surges and retreats of the monsoon front as demonstrated in section 4.

d. Seasonal variations

Figure 7a shows the seasonal cycle of disagreement between (re)analysis products for 18 dekads across the monsoon season. There is an increase in disagreement (σ; Fig. 7a, black line) over the period from April to August, and a reduction during September, which matches the climatological northward progression and retreat of the monsoon front. A more rapid increase in σ occurs at the end of May/start of June with a smaller increase in early August. The distribution of the extreme disagreement times across the season (gray line) shows that there is a peak in early June and another in August. It is speculated that the May–June feature is linked to the monsoon preonset where the monsoon flow jumps farther inland prior to the start of the monsoon rains (Sultan and Janicot 2003). This is also a time of year associated with an increased occurrence of dry squall lines and regions of large downdraft convective available potential energy (DCAPE; Marsham et al. 2008). The features in August are likely linked to the position of the ITD, in the poorly observed interior of West Africa (Fig. 1, with the ITD at 15°–25°N at this time of year), and the higher frequency of MCSs producing large cold pools.

Figure 7b shows the same mean σ as in Fig. 7a (black line), but also σ calculated including CFSR (single-dot–dashed line) and σ for 2006 only (double-dot–dashed line). By removing CFSR, the mean σ is reduced by approximately a third (Fig. 7b). When only considering 2006, σ across almost the entire monsoon season is significantly reduced. It is likely that this result is due to the heavy augmentation of the upper-air observation network that formed part of the AMMA field campaign (Parker et al. 2008; Agustí Panareda et al. 2010b).

4. Meteorology of extreme ITD disagreement events

As described in section 3, any period that exceeds the threshold to place it in the top 5% of events is classified
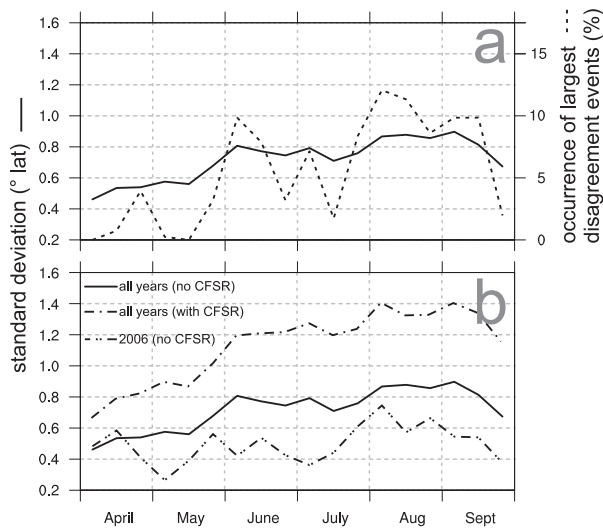
FIG. 7. Seasonal behavior where (a) the mean standard deviation σ for 18 dekads across the monsoon season (solid line) and the percentage of times that it exceeded the extreme disagreement threshold for each of the 18 dekads is shown (dashed line; see section 3 for details). (b) The same mean σ as in (a) (solid line), but with the mean σ calculated including CFSR (single-dot–dashed line) and the σ for 2006 only (double-dot–dashed line).

as an extreme disagreement event. This technique identifies 34 individual events. For each of these, the peak disagreement time was identified (referred to as DAY = 0; henceforth, all other times are relative to the time of peak disagreement). The time at which peak disagreement occurs is not evenly spread across the four (re)analysis time periods (0000, 0600, 1200, and 1800 UTC). There are two events that peak at 0000 UTC, 11 that peak at 0600 UTC, 5 that peak at 1200 UTC, and 16 that peak at 1800 UTC. At least one event occurs in each monsoon season (Fig. 6b). In 2010, 13 extreme events occur, which is far higher than any other year (next highest are 2000 and 2005 with 4 events each), suggesting a greater frequency of the meteorological conditions that lead to strong disagreement. This is also suggested by the fact that the peaks in σ are coincident with large perturbations in the ITDΦ values (Fig. 3).

a. An example ITD disagreement event

Figure 8 shows the meteorological conditions leading up to a peak in disagreement. This event occurred toward the end of July 2010 and can clearly be seen in Fig. 3 as a northward surge of the ITDΦ and a peak in σ. SEVIRI dust imagery and TRMM rainfall retrievals allow for the identification of important meteorological features. The SEVIRI dust imagery is used to diagnose northward surges in the monsoon flow, the production of

convective cloud, and the presence of convective cold pools. This is possible due to its high temporal resolution, the ability to distinguish convective clouds, the tendency for cold pools to lift dust (shown in pink), and a dependence on water vapor, which produces a darker blue in clear-sky conditions during the day when column water vapor is high [this effect can even prevent lifted dust from being detected; Brindley et al. (2012)]. The use of the SEVIRI dust product in this way is subjective and so cannot be used for product verification, but it does give useful information about the development of the monsoon flow for this case.

Figure 8a shows that at 0000 UTC 20 July 2010 (DAY − 4.75) there is a zonally oriented line of MCSs producing heavy precipitation south of 20°N. Over the next day (Figs. 8b,c) a large MCS develops and is positioned over eastern Mali and western Niger. This MCS propagates west and by DAY − 3.75 (Fig. 8c) initiates further convective cells to the north over mountainous regions in southern Algeria and eastern Mali. These new cells grow and form another large MCS (see Figs. 8d,e), which propagates southwestward, producing a TRMM rainfall signal over Mali and Burkina Faso by DAY − 2.25 (Fig. 8f). At this stage SEVIRI imagery shows that there is a large northward surge of moist air behind the MCS (dark blue showing elevated humidity and magenta regions indicating dust lifted by a cold pool). This modification of the low-level moisture distribution by an MCS cold pool is consistent with the event that occurs between 8 and 10 June 2010 studied in Roberts and Knippertz (2014), as well as cases discussed in Cuesta et al. (2010) and Flamant et al. (2007). The region of anomalously moist air over the Sahara remains over parts of Mali, Mauritania, and Algeria and by DAY − 0.75 a group of convective cells is produced as far north as 25°N (Fig. 8g) and continue to grow into an MCS. The northward surge in the ITD moves west with time and beyond DAY − 0.25 (Fig. 8h) becomes less clearly defined through vertical mixing, before returning to a more zonal configuration. This westward movement of the monsoon surge can be seen by the darker blue daytime surface colors and magenta, indicating dust lifted along the edge of the surge in the daytime SEVIRI dust imagery (Figs. 8d,f,h).

This example suggests that the disagreement between (re)analyses is associated with the presence of convective cells. The generation of new cells on the edge or in the wake of an earlier MCS is likely to make the situation more difficult for (re)analyses to represent. In other words, there is little chance that this series of events will be successfully modeled due to the limitations of coarse grids and parameterizations of moist convection. This specific case is also likely to be more difficult to represent
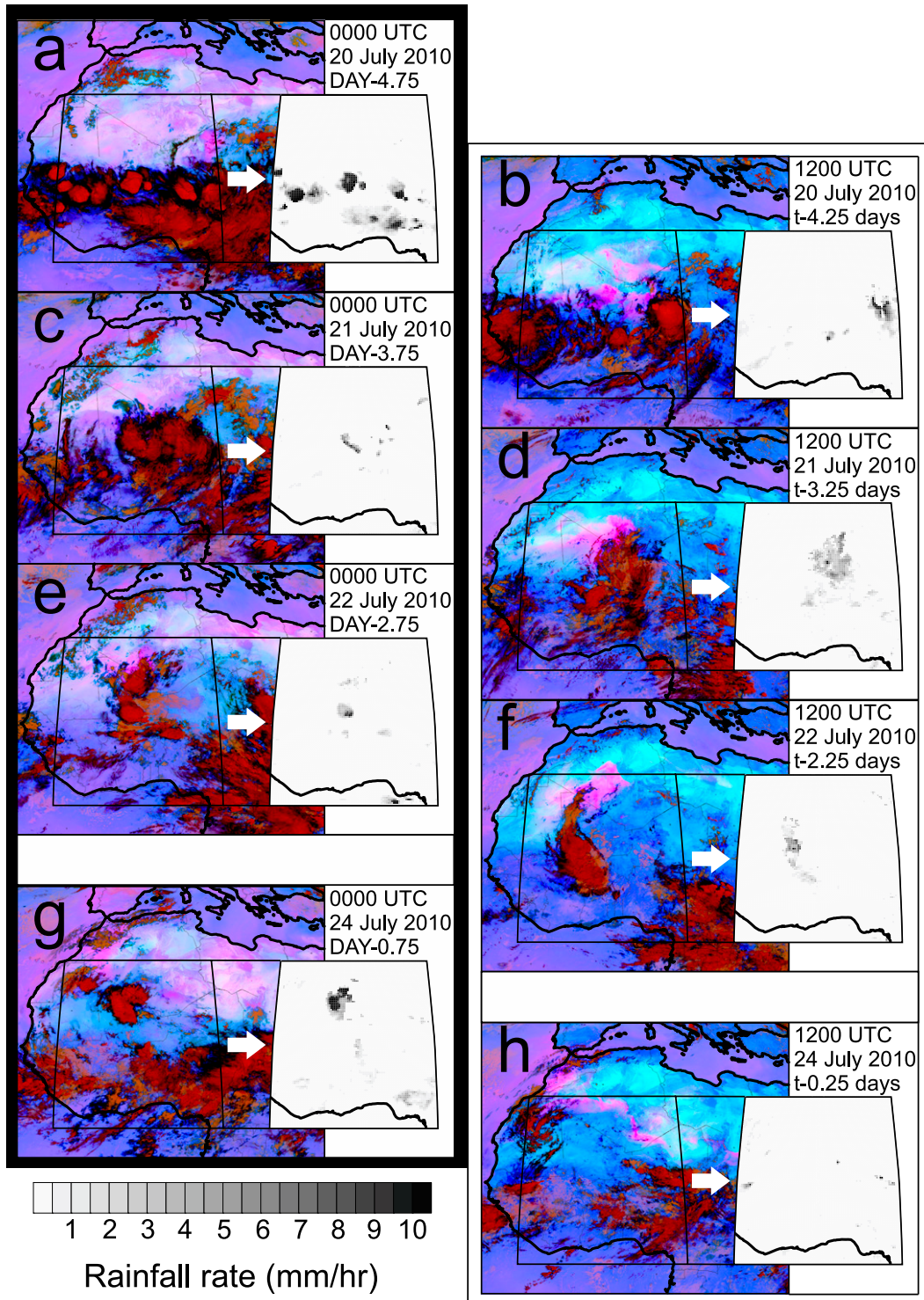
FIG. 8. Development and passage of a northward surge of the monsoon flow, including the production of numerous convective cells within the surge. Shown are SEVIRI dust images (color shading) and TRMM 3B42 rainfall retrievals (inset, gray shading) for (a) 0000 and (b) 1200 UTC 20 Jul, (c) 0000 and (d) 1200 UTC 21 Jul, (e) 0000 and (f) 1200 UTC 22 Jul, and (g) 0000 and (h) 1200 UTC 24 Jul 2010. The color of the borders and the offset in position indicate the time of day (left column for 0000 UTC, black border; and right column for 1200 UTC, white border) and the gray panels between (e) and (g) and (f) and (h) indicate a gap of 2 days instead of 1 day between images. The box shown on the SEVIRI images and bounding the TRMM retrievals is the region being studied and is the same box as shown in Fig. 1 (3°–28°N and 12°W–12°E).
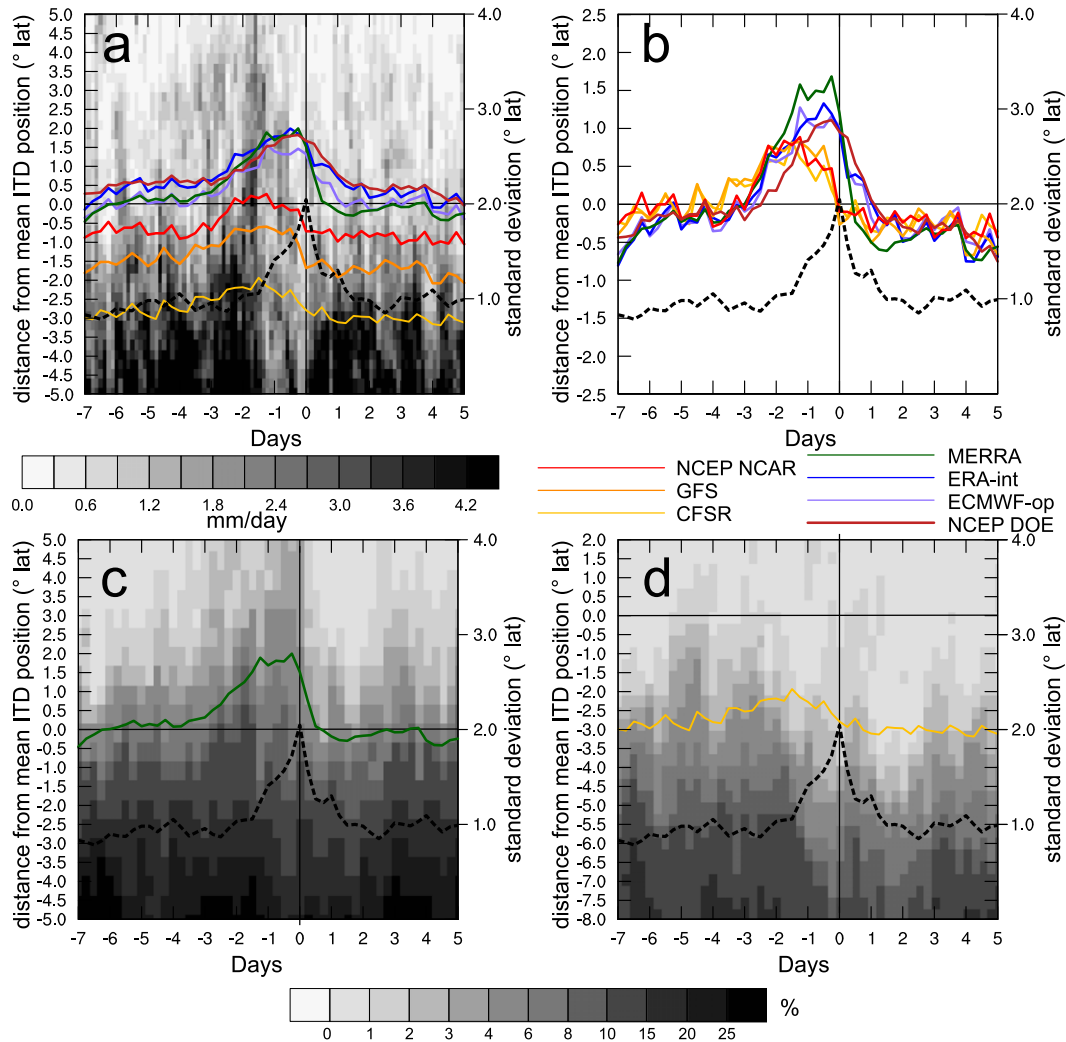
FIG. 9. Composite plots of the 34 events that exceed the standard deviation threshold. All panels show 7 days preceding and 5 days following the time of peak disagreement. (a) The composite position of each of the products' zonal mean ITDΦ during extreme disagreement events relative to a 12-day ensemble mean ITDΦ (colored lines). Also shown is a time–latitude Hovmöller plot of TRMM 3B42 V7 rainfall retrievals for the area shown in the box in Fig. 1 at 3-hourly intervals (gray shading). (b) The ITDΦs for each product plotted relative to their own 12-day mean values, therefore showing the behavior of the ITDΦs rather than absolute position. Hovmöller diagrams of the frequency of cold clouds below −40°C in (c) MERRA and (d) CFSR. The colored lines in (c) and (d) are the same as those plotted in (a) and the dashed black lines in all plots show the same composite standard over the 12-day period.

as later convective cells are initiated in very data-sparse regions.

b. Composites of ITD disagreements

1) BEHAVIOR OF THE ZONAL-MEAN ITD

Figure 9a is a composite plot of the 7 days preceding and 5 days following the peak disagreement time (DAY = 0) of the 34 disagreement events identified. The grayscale shading represents a time–latitude Hovmöller plot of TRMM 3B42 V7 rainfall for the area within the box shown in Fig. 1 at 3-hourly intervals. The latitudinal

position of rainfall is plotted relative to an ITDΦ value averaged across all products and over the 12-day period. This 12-day ensemble mean varies between 13.6° and 21.9°N over the 34 events and has a mean value of 17.8°N. The colored lines show the position of the ITDΦ for each product plotted relative to the same 12-day ensemble mean. These lines give a good idea of the relative position of each of the products when compared to one another and how they compare to the position and strength of the TRMM rainfall. Despite the uneven distribution of (re)analysis times that are assigned as DAY = 0 (see section 4), the diurnal component of the signal is largely

masked and the colored lines predominantly show the synoptic-scale influence on the different ITDΦs. The dashed black line represents the mean σ across all 34 events.

Figure 9a shows that the ITDΦ in CFSR is likely to be positioned approximately 3° south of most of the other products. This offset is in agreement with that shown in Fig. 5a. Also, as expected from Figs. 5d and 6a, the GFS ITDΦ is 1.5° farther south than are most other products. Unexpectedly, however, there is also an offset in the NCEP–NCAR ITDΦ during these events of approximately 0.75° south of the main group of products. To illustrate the range and timing of the movement of the ITDΦ in different products rather than its absolute position, they have also been plotted relative to their own 12-day mean ITDΦ rather than the 12-day ensemble mean (Fig. 9b). Note that σ (dashed black line) remains the same as in Fig. 9a. In all seven products the composite ITDΦ moves north prior to DAY = 0. In CFSR and GFS this northward movement is gradual over the period from DAY − 7 to DAY − 2. However, in the rest of the products, the ITDΦ maintains its position until approximately DAY − 4 at which point a northward surge of the monsoon flow commences. This agrees well with the example shown in Fig. 8. From DAY − 7 to DAY − 2, σ is relatively stable at around 1° latitude (larger than the long-term mean; Figs. 6 and 7). This includes the first 2 days of the northward surge of the ITDΦ seen in most of the (re)analyses. However, between DAY − 2 and DAY = 0, σ increases rapidly during the northward surge and the start of the retreat of the ITDΦs. In Fig. 9b, ERA-Int, NCEP–DOE, and MERRA all show that the ITDΦs continue to move north, reaching a maxima at DAY − 0.25. ECMWF-op behaves similarly but peaks at DAY − 1.25 and maintains its ITDΦ position until the start of a rapid retreat at the same time as seen in ERA-Int, NCEP–DOE, and MERRA. The ITDΦs in NCEP–NCAR and GFS plateau at DAY − 2.25 and then start to retreat at the same time as the products already discussed. The ITDΦ in CFSR starts to retreat at DAY − 2 without having moved very far north compared to other products.

The fact that σ remains relatively low during the initial stage of the northward motion of the ITDΦ could be due to one of three reasons: 1) the important processes are synoptic scale in nature and therefore are satisfactorily resolved, even with the coarse grids used in the (re)analyses; 2) the assimilation of observations is sufficient to constrain the products despite possible differences between their short-term forecasts; or 3) that none of the products represent the situation well because of similar problems with dynamics, but they converge on a single incorrect answer, and there are insufficient observations to correct the first guesses. Currently, it is difficult to say which of these options is most likely. There is also a chance that different events within the composite have good agreement levels at this stage for different reasons.

2) RAINFALL

TRMM rainfall shown in Fig. 9a reveals the production of heavy rainfall south of the ITDΦ between DAY − 6 to DAY − 1.5, suggesting the presence of MCSs. This agrees well with the example discussed in section 4 (Fig. 8). Large MCSs produced close to the ITD are able to significantly advance the position of the monsoon flow by the generation of large evaporatively generated cold pool outflows (Flamant et al. 2007; Marsham et al. 2008). However, it is also the case that meteorological features that favor the development of MCSs can be responsible for similar northward surges of the monsoon flow. In particular, the passage of AEWs across West Africa (Berry and Thorncroft 2005; Cuesta et al. 2010) or the formation of tropical plumes is due to interactions with the subtropical jet stream that enhance southerly flow (Roberts and Knippertz 2014).

The composite TRMM rainfall retrievals have values in excess of 3 mm day^{-1} north of all the products' ITDΦs. The presence of MCSs to the south of the ITDΦs, followed by an increased likelihood of rainfall in the north, points toward incursions of moist air into the northern Sahel and southern Sahara. This might allow for convective triggering in areas that are usually too dry, as is shown in the example in Fig. 8. After this northern rainfall, σ rapidly increases because of the different patterns of ITDΦ behavior described above. This suggests a link between the unusual rainfall observed during TRMM and the large disagreement produced by the differing behaviors visible in Fig. 9b.

Two of the most extreme examples are MERRA and CFSR. MERRA shows a wide range of ITDΦ movement (approximately 2.5° latitude), behaves similarly to three other products (ERA-Int, ECMWF-op, and NCEP–DOE), and has an ITDΦ that continues to move north after the production of rain north of its ITDΦ. CFSR has a small range of ITDΦ movement (approximately 1° latitude), behaves similarly to GFS and NCEP–NCAR (despite the differences in absolute ITDΦ position; see Fig. 9b), and shows a southward retreat in ITDΦ after the production of rain in the north. Figures 9c,d show the ITDΦs for MERRA and CFSR (colored lines) while the grayscale shading shows a time–latitude Hovmöller diagram of the frequency of model outgoing longwave radiation values that equate to cloud-top temperatures of −40°C or colder (assuming an emissivity of 1). This method has been employed because of the dependence of TRMM rainfall retrievals on cloud-top temperature and the fact that the deep dry

boundary layer in the Sahel and Sahara has the potential to limit the amount of rainfall that reaches the surface. These are both plotted relative to the same 12-day ensemble mean ITDΦ used in Fig. 9a and so can be directly compared to the TRMM rainfall Hovmöller plot shown in Fig. 9a (note that the window for Fig. 9d has been shifted to center on the CFSR ITDΦ).

Rainfall in the TRMM retrievals (Fig. 9a), south of all the ITDΦs between DAY − 6 and DAY − 1.5, should correspond to regions of cold cloud in Figs. 9c,d. In fact, the shading in Fig. 9c suggests that MERRA does represent the MCSs responsible for rainfall here. A similar pattern can also be seen in Fig. 9d for CFSR but is less well defined. Also, because of the offset in the position of the ITDΦ, the cold cloud occurs significantly farther south than is seen in the observations. Another similarity between MERRA and TRMM Hovmöller plots is the increased frequency of rainfall/cold cloud close to and even north of the ITDΦ. There are, however, some differences in the distributions. Notably, TRMM rainfall suggests that relatively heavy rain is likely north of the ITDΦs between DAY − 3.5 and DAY − 1. In contrast, the increased frequency of cold cloud at these latitudes is weaker in MERRA (an equivalent period of cold cloud is not present in CFSR). Another difference between TRMM and MERRA is that cold cloud north of the ITDΦ persists until DAY = 0, while there is very little TRMM rainfall in this region after DAY − 1. This suggests that the rapid growth and collapse of convective cells, likely responsible for this rainfall (Fig. 9a), is not well represented by the convective parameterizations in MERRA. Also, in the TRMM retrievals there is a large reduction in the amount of rainfall over almost the entire 10°-latitude range of the Hovmöller plot and a much weaker north–south gradient between DAY − 1.5 and DAY + 0.5. During the same period MERRA and CFSR still display strong north–south gradients of cold cloud frequency and a much less pronounced reduction in cold cloud in the south. The overall greater success of MERRA in reproducing the evolution of the cold cloud compared with TRMM rainfall, in particular the production of cloud north of the ITDΦ at DAY − 1, suggests that the greater northward shift in the ITDΦ in MERRA compared with CFSR is perhaps more realistic, although further research would be needed to confirm this.

All of the differences discussed above highlight the need to improve the (re)analyses. One possible avenue is by the assimilation of clouds into three-/four-dimensional variational data assimilation (3D/4DVAR) systems. Storto and Tveter (2009) illustrate how a pseudo-observation assimilation scheme using *CloudSat* data has a clear benefit on a number of different fields in a 3DVAR assimilation scheme. They also suggest that the

technique might be extended to be used for other sources of data including satellite-borne infrared sensors. More recently, Kostka et al. (2014) have presented work aimed at utilizing both visible and near-infrared data to increase the amount of information about clouds that can be assimilated.

3) DUST UPLIFT

We can see from Fig. 8 and the event studied in Roberts and Knippertz (2014) that periods that display disagreement in low-level moisture over West Africa can also be linked to the lifting of dust. This primarily appears to be due to the formation of haboobs, where dust is lifted by the turbulent winds associated with evaporatively generated cold pools from MCSs. Figure 10 shows composites of Moderate Resolution Imaging Spectroradiometer (MODIS) Deep Blue aerosol optical depth (AOD) (top of each panel), AOD anomaly (bottom of each panel), and TRMM rainfall (grayscale inset within each panel) for the 34 extreme disagreement events. Composite 925-hPa geopotential and the position of the ITD based on the $10 \, \mathrm{g \, kg^{-1}} \, q_{925}$ isopleth from ERA-Int are also shown. Anomalies are calculated with respect to an 11-yr period of MODIS AOD using a 31-day triangular window filter to produce a smoothed climatology.

Figure 10a shows that on DAY − 5 there are elevated AOD values over the western coast, southern Algeria, Niger and western Chad. The AOD anomalies for this day are high in both the coastal region and over Algeria north of the $10 \, \mathrm{g \, kg^{-1}} \, q_{925}$ isopleth. However, over Niger and Chad the dust uplift is close to the climatology or is anomalously low. The position of the SHL suggests that the anomalously strong AODs are generated by the lifting of dust by low-level jets over Algeria (e.g., Birch et al. 2013) and the strong winds linked to the Atlantic inflow region over western Sahara and Mauritania (e.g., Grams et al. 2010). The composite TRMM rainfall for DAY − 5 indicates a strong north–south gradient with less rain in the north and more in the south of the box.

Figure 10b shows how the AOD and meteorology develop over a 2-day period. The SHL weakens and its center moves west toward the coast, which is consistent with the behavior of the SHL documented by Lavaysse et al. (2010) and Roehrig et al. (2011). Over the same period the edge of the monsoon flow moves northward over Mauritania, Mali, and Algeria. AOD anomalies associated with the circulation of air around the SHL weaken (AOD anomalies are negative over southern Algeria north of the $10 \, \mathrm{g \, kg^{-1}} \, q_{925}$ isopleth; Fig. 10b). Composite TRMM rainfall indicates that there is more intense rainfall in the southern half of the box and an increase in rainfall within the northward bulge of the monsoon flow.
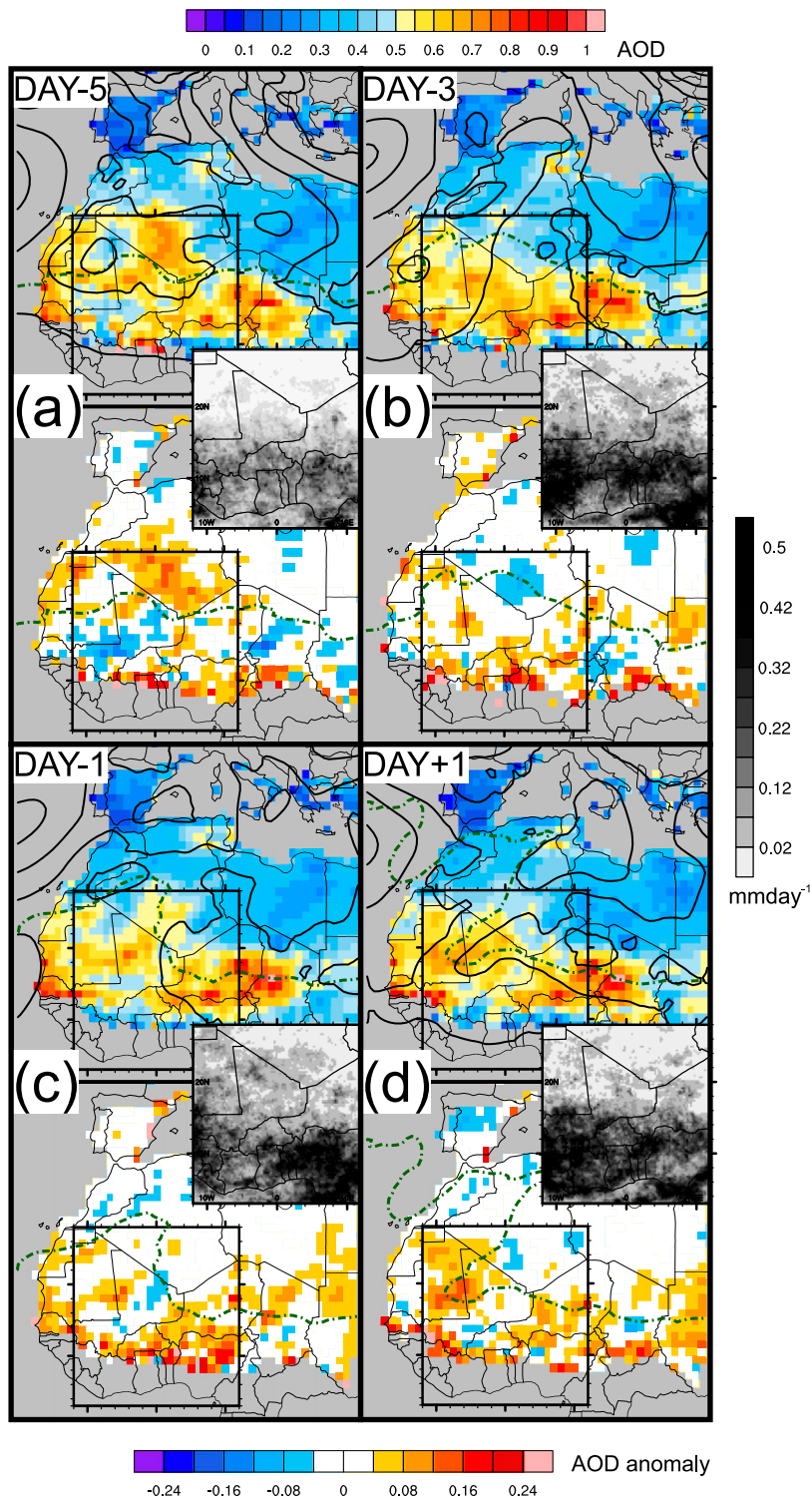
FIG. 10. Composites showing important meteorological features and atmospheric aerosol features for events that exceed the standard deviation threshold. Shown are MODIS Deep Blue AOD (color shading at top of each panel), AOD anomaly (color shading at bottom of each panel), TRMM 3B42 V7 rainfall (gray shading inset), ERA-Int 925-hPa geopotential (black lines at top of each panel), and position of ITD from q_{925} $10 \, g \, kg^{-1}$ isopleth (dashed green line). Composites are shown for (a) DAY $-$ 5, (b) DAY $-$ 3, (c) DAY $-$ 1, and (d) DAY $+$ 1 from the 34 extreme disagreement events.

Two days later at DAY − 1 (the day prior to peak disagreement during the strongest northerly rainfall signal; Fig. 10c) the SHL in the west continues to weaken and the northward bulge of the ITD moves westward in a similar manner to that shown in Fig. 8. In the east another SHL center has formed and produces higher AOD values linked to the Bodélé Depression across the Niger–Chad border. In the west of the box the monsoon flow reaches very far north. Composite TRMM precipitation indicates that there is still strong rainfall in the southeast of the domain but that rainfall in the southwest has weakened. There is also increased retrieved rainfall in the northwestern part of the box (coincident with the region covered by the monsoon surge). The relatively small response to this rainfall on DAY − 1 could be partly related to detection problems of dust under cloud. In addition, the MODIS Deep Blue AOD product is based solely on daytime overpasses making dust lifted by haboobs (which usually occur in the evening and overnight) more likely to be detected the following day.

By DAY + 1 (Fig. 10d) the northward surge of the monsoon flow has begun to break down as it moves west and there is a more usual position of the ITD in the eastern part of the box. Also, the SHL center in the east has begun to deepen and spread west. Composite TRMM data indicates that rainfall in the northern half of the box has weakened and there is a very strong north–south gradient in precipitation. At this time high AOD values are widespread over Mauritania and Mali, coincident with the position of the unusual rainfall in the northwest of the box shown in Fig. 10c. This represents a significant anomaly in spatial extent and magnitude and suggests that the production of haboobs when (re)analyses are in disagreement is responsible for strongly anomalous dust uplift over Mauritania and Mali.

5. Summary and conclusions

This paper investigates the differences in low-level moisture distribution over West Africa in seven different reanalysis and operational analysis products (see section 2) during 11 consecutive monsoon seasons (April–September 2000–10). This work 1) identifies periods of the largest disagreement, 2) discusses the interannual and seasonal patterns of disagreement, and 3) analyzes the meteorology and impact on dust of the episodes that display the strongest disagreement.

The largest differences in low-level humidity over West Africa tend to be near the ITD and are likely caused by disagreements over the position of the monsoon front rather than regional moisture biases. The scale of these differences can be large, often over 50% of the total q_{925}

values typical of the Sahel and Sahara. Products that have similar model physics and data assimilation methods (e.g., products from the same centers) show smaller q_{925} differences compared to other (re)analyses.

CFSR has a systematic bias in its zonal mean ITD position (ITDΦ), being 100–200 km farther south than the other products studied. This bias is reduced slightly over the period studied. GFS displays a similar bias to CFSR during the years 2000 and 2007–10. The NCEP–DOE ITDΦ is characterized by marked northerly outliers compared to the mean ITDΦ from the other products. The year 2006 stands out as a year with very low disagreement between (re)analyses, most likely due to enhanced upper-air observations during the AMMA field campaign. The two years with the highest levels of disagreement are 2000 and 2010. The increased disagreement in 2000 is associated with the bias present in GFS. In 2010 the occurrence of a large number of extreme events compared to other years (13 compared to 4 in the next highest years) produces high levels of disagreement between products.

Seasonally, the disagreement increases from April to August with periods of particular disagreement occurring in late May/early June and August. The May–June feature is coincident with the monsoon preonset. The August feature is likely produced by the ITD being positioned in the poorly observed interior of West Africa and a higher frequency of cold-pool-producing MCSs.

The extreme events identified are linked to northward surges of the ITDΦ and usually coincide with the subsequent southward return of the same feature. During disagreement events the NCEP–DOE, MERRA, ERA-Int, and ECMWF-op ITDΦs are closely grouped. There are southward offsets from this group of approximately 3°, 1.5°, and 0.75° in CFSR, GFS, and NCEP–NCAR, respectively. Relatively low disagreement during the first few days of the surge are due to either 1) important processes being synoptic scale and satisfactorily resolved in (re)analyses, 2) assimilation of observations being sufficient to constrain the products, or 3) all products failing to represent reality but being convergent on a single incorrect representation of the atmosphere. It is assumed here that specific meteorological conditions make it particularly hard to produce a consistent ensemble of (re)analyses leading to situations of large disagreement. Special caution should be used when employing any product in isolation at such times. Investigating periods of disagreement, and the weather associated with them, gives clues as to the process errors leading to model deviation. This motivates future work into improving the representation of these processes and research into identifying which products perform better at such times. There is a link between extreme disagreement events and the

presence of convective cells. TRMM indicates precipitation north of the ITDΦs up to 4 days prior to the time of peak disagreement. Poor representation and assimilation of the effects of convective cells within a northward perturbation of the ITD is a possible mechanism leading to product disagreement.

The representation of cold cloud in MERRA and CFSR is compared with TRMM precipitation. The cold cloud distribution in MERRA is similar to the rainfall from TRMM. The cold cloud distribution in CFSR compares less favorably with clouds too far south and a smaller cold cloud signal north of the ITDΦ. TRMM precipitation is reduced the day before the peak disagreement and the north–south gradient is much weaker than at other times. MERRA and CFSR show much less pronounced reductions in cold cloud and retain strong north–south gradients.

It is difficult to disentangle whether northward surges of the ITD are produced by the generation of cold pools by MCSs, or as a result of synoptic-scale features that also encourage convective triggering (e.g., AEWs, subtropical disturbances). Both probably contribute through the life cycle of the surges; however, their relative importance remains unknown. The (re)analysis models rely on parameterized convection and do not create propagating MCSs or cold pool outflows. Therefore, our finding that the presence of MCSs is linked to disagreement in the low-level moisture distribution over West Africa is consistent with the known process errors in modeled moist convection. The shortage of data in West Africa means that the model errors cannot be sufficiently corrected by the assimilation of observation data. Monsoon surges are a major mechanism for dust mobilization and this work underlines the difficulty of using (re)analyses to estimate dust uplift [see also Marsham et al. (2011) and Heinold et al. (2013)]. This is especially true given that it has been shown that periods of disagreement are likely to be associated with anomalously dusty conditions.

Moreover, this study highlights the importance of upper-air observations over West Africa for robust (re)analyses. The AMMA campaign has shown that improvements in the upper-air observation network are possible and can in some cases be relatively inexpensive (Parker et al. 2008), but sufficient funds and staff are required. The shortage of radiosonde data makes effective use of satellite data particularly important: the use of novel techniques such as those discussed in Storto and Tveter (2009) and Kostka et al. (2014) are of particular interest as there is potential for improved representation of subgrid-scale processes in (re)analyses for a relatively small investment.

REFERENCES

Agustí Panareda, A., and Coauthors, 2010a: The ECMWF re-analysis for the AMMA observational campaign. *Quart. J. Roy. Meteor. Soc.,* **136,** 1457–1472, doi:10.1002/qj.662.

——, A. Beljaars, C. Cardinali, I. Genkova, and C. Thorncroft, 2010b: Impacts of assimilating AMMA soundings on ECMWF analyses and forecasts. *Wea. Forecasting,* **25,** 1142–110, doi:10.1175/2010WAF2222370.1.

Bain, C. L., D. J. Parker, N. Dixon, A. H. Fink, C. M. Taylor, B. Brooks, and S. F. Milton, 2011: Anatomy of an observed African easterly wave in July 2006. *Quart. J. Roy. Meteor. Soc.,* **137B,** 923–933, doi:10.1002/qj.812.

Berry, G., and C. D. Thorncroft, 2005: Case study of an intense African easterly wave. *Mon. Wea. Rev.,* **133,** 752–766, doi:10.1175/MWR2884.1.

Birch, C. E., D. J. Parker, A. O'Leary, J. H. Marsham, C. M. Taylor, P. P. Harris, and G. M. S. Lister, 2013: Impact of soil moisture and convectively generated waves on the initiation of a West African mesoscale convective system. *Quart. J. Roy. Meteor. Soc.,* **139,** 1712–1730, doi:10.1002/qj.2062.

Bou Karam, D., C. Flamant, P. Knippertz, O. Reitebuch, J. Pelon, M. Chong, and A. Dabas, 2008: Dust emissions over the Sahel associated with the West African monsoon intertropical discontinuity region: A representative case-study. *Quart. J. Roy. Meteor. Soc.,* **134,** 621–634, doi:10.1002/qj.244.

Brindley, H., P. Knippertz, C. Ryder, and I. Ashpole, 2012: A critical evaluation of the ability of the Spinning Enhanced Visible and Infrared Imager (SEVIRI) thermal infrared red-green-blue rendering to identify dust events: Theoretical analysis. *J. Geophys. Res.,* **117,** D07201, doi:10.1029/2011JD017326.

Burton, R. R., G. M. Devine, D. J. Parker, P. Chazette, N. Dixon, C. Flamant, and J. M. Haywood, 2013: The Harmattan over West Africa: Nocturnal structure and frontogenesis. *Quart. J. Roy. Meteor. Soc.,* **139,** 1364–1373, doi:10.1002/qj.2036.

Chipperfield, M. P., 2006: New version of the TOMCAT/SLIMCAT off-line chemical transport model: Intercomparison of stratospheric tracer experiments. *Quart. J. Roy. Meteor. Soc.,* **132,** 1179–1203, doi:10.1256/qj.05.51.

Couvreux, F., F. Guichard, O. Bock, B. Campistron, J. P. Lafore, and J. L. Redelsperger, 2010: Synoptic variability of the monsoon flux over West Africa prior to the onset. *Quart. J. Roy. Meteor. Soc.,* **136** (S1), 159–173, doi:10.1002/qj.473.

Cuesta, J., C. Lavaysse, C. Flamant, M. Mimouni, and P. Knippertz, 2010: Northward bursts of the West African monsoon leading to rainfall over the Hoggar Massif, Algeria. *Quart. J. Roy. Meteor. Soc.,* **136** (S1), 174–189, doi:10.1002/qj.439.

Dee, D. P., and Coauthors, 2011: The ERA-Interim reanalysis: Configuration and performance of the data assimilation system. *Quart. J. Roy. Meteor. Soc.,* **137,** 553–597, doi:10.1002/qj.828.

Emmons, L. K., and Coauthors, 2010: Description and evaluation of the Model for Ozone and Related chemical Tracers, version 4 (MOZART-4). *Geosci. Model Dev.,* **3,** 43–67, doi:10.5194/gmd-3-43-2010.

Flamant, C., J.-P. Chaboureau, D. Parker, C. Taylor, J.-P. Cammas, O. Bock, F. Timouk, and J. Pelon, 2007: Airborne observations of the impact of a convective system on the planetary boundary layer thermodynamics and aerosol distribution in the intertropical discontinuity region of the West African monsoon. *Quart. J. Roy. Meteor. Soc.,* **133,** 1175–1189, doi:10.1002/qj.97.

Garcia-Carreras, L., and Coauthors, 2013: The impact of convective cold pool outflows on model biases in the Sahara. *Geophys. Res. Lett.,* **40,** 1647–1652, doi:10.1002/grl.50239.

Grams, C. M., S. C. Jones, J. H. Marsham, D. J. Parker, J. M. Haywood, and V. Heuveline, 2010: The Atlantic inflow to the Saharan heat low: Observations and modelling. *Quart. J. Roy. Meteor. Soc.,* **136** (S1), 125–140, doi:10.1002/qj.429.

Hamilton, R. A., J. W. Archbold, and C. K. M. Douglas, 1945: Meteorology of Nigeria and adjacent territory. *Quart. J. Roy. Meteor. Soc.,* **71,** 231–264, doi:10.1002/qj.49707130905.

Heinold, B., P. Knippertz, J. H. Marsham, S. Fiedler, N. S. Dixon, K. Schepanski, B. Laurent, and I. Tegen, 2013: The role of deep convection and nocturnal low-level jets for dust emission in summertime West Africa: Estimates from convection-permitting simulations. *J. Geophys. Res. Atmos.,* **118,** 4385–4400, doi:10.1002/jgrd.50402.

Huffman, G. J., and Coauthors, 2007: The TRMM Multisatellite Precipitation Analysis (TMPA): Quasi-global, multiyear, combined-sensor precipitation estimates at fine scales. *J. Hydrometeor.,* **8,** 38–55, doi:10.1175/JHM560.1.

Huijnen, V., and Coauthors, 2010: The global chemistry transport model TM5: Description and evaluation of the tropospheric chemistry version 3.0. *Geosci. Model Dev.,* **3,** 1009–1087, doi:10.5194/gmdd-3-1009-2010.

Janiga, M. A., and C. D. Thorncroft, 2013: Regional differences in the kinematic and thermodynamic structure of African easterly waves. *Quart. J. Roy. Meteor. Soc.,* **139,** 1598–1614, doi:10.1002/qj.2047.

Kalnay, E., and Coauthors, 1996: The NCEP/NCAR 40-Year Reanalysis Project. *Bull. Amer. Meteor. Soc.,* **77,** 437–471, doi:10.1175/1520-0477(1996)077<0437:TNYRP>2.0.CO;2.

Kanamitsu, M., W. Ebisuzaki, J. Woollen, S.-K. Yang, J. J. Hnilo, M. Fiorino, and G. L. Potter, 2002: NCAP–DOE AMIP-II Reanalysis (R-2). *Bull. Amer. Meteor. Soc.,* **83,** 1631–1643, doi:10.1175/BAMS-83-11-1631.

Kistler, R., and Coauthors, 2001: The NCEP–NCAR 50-Year Reanalysis: Monthly means CD-ROM and documentation. *Bull. Amer. Meteor. Soc.,* **82,** 247–267, doi:10.1175/1520-0477(2001)082<0247:TNNYRM>2.3.\CO;2.

Knippertz, P., 2008: Dust emissions in the West African heat trough—The role of the diurnal cycle and of extratropical disturbances. *Meteor. Z.,* **17,** 553–563, doi:10.1127/0941-2948/2008/0315.

——, and J. E. Martin, 2005: Tropical plumes and extreme precipitation in subtropical and tropical West Africa. *Quart. J. Roy. Meteor. Soc.,* **131,** 2337–2365, doi:10.1256/qj.04.148.

——, and M. C. Todd, 2010: The central west Saharan dust hot spot and its relation to African easterly waves and extratropical disturbances. *J. Geophys. Res.,* **115,** D12117, doi:10.1029/2009JD012819.

——, and ——, 2012: Mineral dust aerosols over the Sahara: Meteorological controls on emission and transport and implications for modeling. *Rev. Geophys.,* **50,** RG1007, doi:10.1029/2011RG000362.

——, J. Trentmann, and A. Seifert, 2009: High-resolution simulations of convective cold pools over the northwestern Sahara. *J. Geophys. Res.,* **114,** D08110, doi:10.1029/2008JD011271.

Kostka, P. M., M. Weissmann, R. Buras, B. Mayer, and O. Stiller, 2014: Observation operator for visible and near-infrared satellite reflectances *J. Atmos. Oceanic Technol.,* **31,** 1216–1233, doi:10.1175/JTECH-D-13-00116.1.

Lavaysse, C., C. Flamant, S. Janicot, and P. Knippertz, 2010: Links between African easterly waves, midlatitude circulation and intraseasonal pulsations of the West African heat low. *Quart. J. Roy. Meteor. Soc.,* **136,** 141–158, doi:10.1002/qj.555.

Lorenz, C. and H. Kunstmann, 2012: The hydrological cycle in three state-of-the-art reanalyses: Intercomparison and performance analysis. *J. Hydrometeor.,* **13,** 1397–1420, doi:10.1175/JHM-D-11-088.1.

Marsham, J. H., D. J. Parker, C. M. Grams, C. M. Taylor, and J. M. Haywood, 2008: Uplift of Saharan dust south of the intertropical discontinuity. *J. Geophys. Res.,* **113,** D21102, doi:10.1029/2008JD009844.

——, P. Knippertz, N. S. Dixon, D. J. Parker, and G. M. S. Lister, 2011: The importance of the representation of deep convection for modeled dust-generating winds over West Africa during summer. *Geophys. Res. Lett.,* **38,** L16803, doi:10.1029/2011GL048368.

——, N. S. Dixon, L. Garcia-Carreras, G. M. S. Lister, D. J. Parker, P. Knippertz, and C. E. Birch, 2013a: The role of moist convection in the West African Monsoon system: Insights from continental-scale convection-permitting simulations. *Geophys. Res. Lett.,* **40,** 1843–1849, doi:10.1002/grl.50347.

——, and Coauthors, 2013b: Meteorology and dust in the central Sahara: Observations from Fennec supersite-1 during the June 2011 intensive observation period. *J. Geophys. Res. Atmos.,* **118,** 4069–4089, doi:10.1002/jgrd.50211.

Mekonnen, A., C. D. Thorncroft, A. R. Aiyyer, and G. N. Kiladis, 2008: Convectively coupled Kelvin waves over tropical Africa during the boreal summer: Structure and variability. *J. Climate,* **21,** 6649–6667, doi:10.1175/2008JCLI2008.1.

Mera, R., A. G. Laing, and F. Semazzi, 2014: Moisture variability and multiscale interactions during spring in West Africa. *Mon. Wea. Rev.,* **142,** 3178–3198, doi:10.1175/MWR-D-13-00175.1.

Mohr, K. I., J. S. Famiglietti, and E. J. Zipser, 1999: The contribution to tropical rainfall with respect to convective system type, size, and intensity estimated from the 85-GHz ice-scattering signature. *J. Appl. Meteor.,* **38,** 596–606, doi:10.1175/1520-0450(1999)038<0596:TCTTRW>2.0.CO;2.

Mounier, F., G. N. Kiladis, and S. Janicot, 2007: Analysis of the dominant mode of convectively coupled Kelvin waves in the West African monsoon. *J. Climate,* **20,** 1487–1503, doi:10.1175/JCLI4059.1.

Pandya, R., and Coauthors, 2015: Using weather forecasts to help manage meningitis in the West African Sahel. *Bull. Amer. Meteor. Soc.,* doi:10.1175/BAMS-D-13-00121.1, in press.

Parker, D. J., and Coauthors, 2005: The diurnal cycle of the West African monsoon circulation. *Quart. J. Roy. Meteor. Soc.,* **131,** 2839–2860, doi:10.1256/qj.04.52.

——, and Coauthors, 2008: The AMMA radiosonde program and its implications for the future of atmospheric monitoring over Africa. *Bull. Amer. Meteor. Soc.,* **89,** 1015–1027, doi:10.1175/2008BAMS2436.1.

Pospichal, B., D. Bou Karam, S. Crewell, C. Flamant, A. Hünerbein, O. Bock, and F. Saïd, 2010: Diurnal cycle of the intertropical discontinuity over West Africa analysed by remote sensing and mesoscale modelling. *Quart. J. Roy. Meteor. Soc.,* **136** (S1), 92–106, doi:10.1002/qj.435.

Reinfried, F., I. Tegen, B. Heinold, O. Hellmuth, K. Schepanski, U. Cubasch, H. Huebener, and P. Knippertz, 2009: Simulations of convectively driven density currents in the Atlas region using a regional model: Impacts on dust emission and sensitivity to horizontal resolution and convection schemes. *J. Geophys. Res.,* **114,** D08127, doi:10.1029/2008JD010844.

Rienecker, M. M., and Coauthors, 2008: The GEOS-5 Data Assimilation System—Documentation of versions 5.0.1, 5.1.0, and 5.2.0. NASA Tech. Rep. NASA/TM-2008-104606, Tech. Rep. Series on Global Modeling and Data Assimilation, Vol. 27, 98 pp. [Available online at http://gmao.gsfc.nasa.gov/pubs/docs/Rienecker369.pdf.]

——, and Coauthors, 2011: MERRA: NASA's Modern-Era Retrospective Analysis for Research and Applications. *J. Climate,* **24,** 3624–3648, doi:10.1175/JCLI-D-11-00015.1.

Roberts, A., and P. Knippertz, 2012: Haboobs: Convectively generated dust storms in West Africa. *Weather,* **67** (12), 311–316, doi:10.1002/wea.1968.

——, and ——, 2014: The formation of a large summertime Saharan dust plume: Convective and synoptic-scale analysis. *J. Geophys. Res. Atmos.,* **119,** 1766–1785, doi:10.1002/2013JD020667.

Roehrig, R., F. Chauvin, and J.-P. Lafore, 2011: 10–25-day intraseasonal variability of convection over the Sahel: A role of the Saharan heat low and midlatitudes. *J. Climate,* **24,** 5863–5878, doi:10.1175/2011JCLI3960.1.

Saha, S., and Coauthors, 2010: The NCEP Climate Forecast System Reanalysis. *Bull. Amer. Meteor. Soc.,* **91,** 1015–1057, doi:10.1175/2010BAMS3001.1.

Schepanski, K., P. Knippertz, S. Fiedler, F. Timouk, and J. Demarty, 2014: The sensitivity of nocturnal low-level jets and near-surface winds over the Sahel to model resolution, initial conditions and boundary-layer set-up. *Quart. J. Roy. Meteor. Soc.,* doi:10.1002/qj.2453, in press.

Solomon, S., D. Qin, M. Manning, Z. Chen, M. Marquis, K. Averyt, M. Tignor, and H. L. Miller Jr., Eds., 2007: *Climate Change 2007: The Physical Science Basis.* Cambridge University Press, 996 pp.

Solomos, S., G. Kallos, E. Mavromatidis, and J. Kushta, 2012: Density currents as a desert dust mobilization mechanism. *Atmos. Chem. Phys.,* **12,** 11 199–11 211, doi:10.5194/acp-12-11199-2012.

Storto, A., and F. T. Tveter, 2009: Assimilating humidity pseudo-observations derived from the cloud profiling radar aboard CloudSat in ALADIN 3D-Var. *Meteor. Appl.,* **16,** 461–479, doi:10.1002/met.144.

Sultan, B., and S. Janicot, 2000: Abrupt shift of the ITCZ over West Africa and intra-seasonal variability. *Geophys. Res. Lett.,* **27,** 3353–3356, doi:10.1029/1999GL011285.

——, and ——, 2003: The West African monsoon dynamics. Part II: The preonset and onset of the summer monsoon. *J. Climate,* **16,** 3407–3427, doi:10.1175/1520-0442(2003)016<3407:TWAMDP>2.0.CO;2.

——, ——, and P. Drobinski, 2007: Characterization of the diurnal cycle of the West African monsoon around the monsoon onset. *J. Climate,* **20,** 4014–4032, doi:10.1175/JCLI4218.1.

Sutton, L., 1925: Haboobs. *Quart. J. Roy. Meteor. Soc.,* **51,** 25–30, doi:10.1002/qj.49705121305.

Trenberth, K. E., and C. J. Guillemot, 1995: Evaluation of the global atmospheric moisture budget as seen from analyses. *J. Climate,* **8,** 2255–2272, doi:10.1175/1520-0442(1995)008<2255:EOTGAM>2.0.CO;2.

Urban, J., 2013: Satellite sensors measuring atmospheric water vapour. *Monitoring Atmospheric Water Vapour,* N. Kämpfer, Ed., Springer, 175–214.

Vizy, E. K. and K. H. Cook, 2009: A mechanism for African monsoon breaks: Mediterranean cold air surges. *J. Geophys. Res.,* **114,** D01104, doi:10.1029/2008JD010654.